

MoSca: Dynamic Gaussian Fusion from Casual Videos via 4D Motion Scaffolds

Jiahui Lei¹ Yijia Weng² Adam Harley² Leonidas Guibas² Kostas Daniilidis^{1,3}
¹ University of Pennsylvania ² Stanford University ³ Archimedes, Athena RC
 {leijh, kostas}@cis.upenn.edu, {yijiaw, aharley, guibas}@cs.stanford.edu
<https://www.cis.upenn.edu/~leijh/projects/mosca>

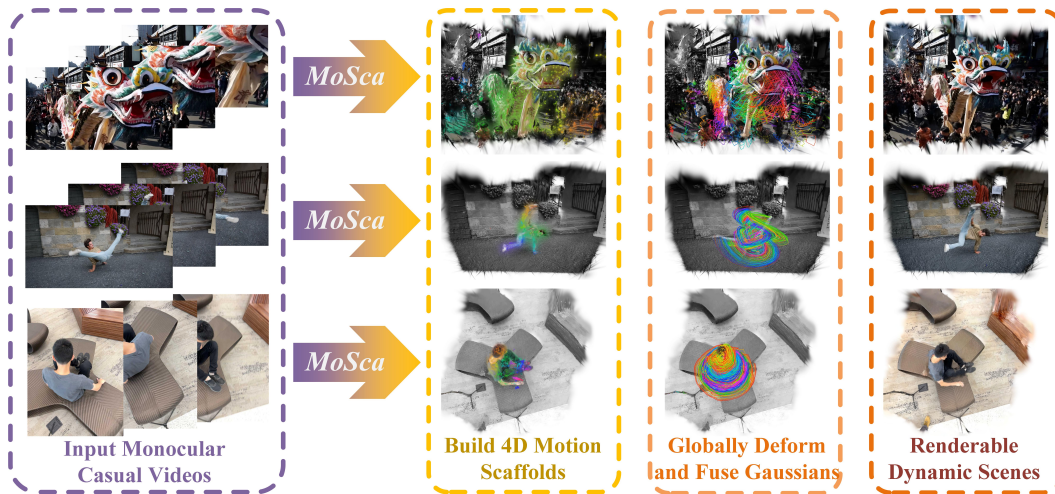


Figure 1: *MoSca* reconstructs renderable dynamic scenes from monocular casual videos.

Abstract

We introduce 4D Motion Scaffolds (MoSca), a neural information processing system designed to reconstruct and synthesize novel views of dynamic scenes from monocular videos captured casually in the wild. To address such a challenging and ill-posed inverse problem, we leverage prior knowledge from foundational vision models, lift the video data to a novel Motion Scaffold (MoSca) representation, which compactly and smoothly encodes the underlying motions / deformations. The scene geometry and appearance are then disentangled from the deformation field, and are encoded by globally fusing the Gaussians anchored onto the MoSca and optimized via Gaussian Splatting. Additionally, camera poses can be seamlessly initialized and refined during the dynamic rendering process, without the need for other pose estimation tools. Experiments demonstrate state-of-the-art performance on dynamic rendering benchmarks. The code will be released no later than the acceptance of this paper.

1 Introduction

The world is dynamic. A fundamental goal of computer vision is to comprehend this dynamic world through spatial intelligence. We propose 4D Motion Scaffolds (*MoSca*), a dynamic scene reconstruction and neural rendering system for casual monocular video inputs with unknown camera poses – the most general in-the-wild data, whose rendering has been proved to be extremely hard and ill-posed [1–3] due to the lack of enough multi-view stereo cues.

To tackle this challenging task, our first insight is to exploit the recent advances of pretrained vision models (Sec. 3.1), which today are very effective at fundamental computer vision tasks

such as tracking and depth estimation. This knowledge provides a critical boost to understanding the complete dynamic scene, but it does not suffice, as it provides no useful information on the occluded part of the scene. Our second insight is to design a deformation representation, *MoSca*, derived from the above foundational priors, exploiting a *physical* deformation prior. Specifically, although the real-world geometry and appearance are complex and include high-frequency details, the underlying deformation that drives these geometries is usually compact (low-rank) and smooth. *MoSca* disentangles the 3D geometry and motion by representing the deformation with sparse graph nodes that can be smoothly interpolated (Sec. 3.2). Another physical prior we exploit is the as-rigid-as-possible (ARAP) deformation, which can be efficiently applied via the topology of *MoSca*. Two important benefits arise from the above two insights: firstly, the tailored *MoSca* can be seamlessly lifted and optimized from the inferred 2D foundational priors (Sec. 3.3), and secondly the observations from all different timesteps can be globally fused to a target rendering timestep (Sec. 3.4). The Gaussian fusion happens when we deform all the different times observed Gaussians to the query time, forming a complete reconstruction, which can be supervised through Gaussian Splatting [4] rendering. Additionally, our system can estimate camera pose via bundle adjustment and the photometric optimization (Sec. 3.5), obviating the need for other poses estimators such as COLMAP.

In summary, our main contributions can be summarized as: (1) A novel Motions Scaffold deformation representation, which we build using knowledge from 2D foundational models, and optimize via physically-inspired deformation regularizations. (2) An efficient and explicit Gaussian-based dynamic scene representation, driven by *MoSca*, which globally fuses observations across an input video to render this data into a viewpoint and timestep of choice. (3) State-of-the-art performance on dynamic scene rendering benchmarks and a COLMAP-free dynamic neural rendering system for casual videos.

2 Related Works

Dynamic Novel-View Synthesis. Novel-view synthesis of dynamic scenes is challenging. Many existing works [5–15] assume available synchronized multi-view video inputs. Another line of works [16–27, 2, 28, 29] tackles the more practical setting of monocular observations. The ambiguity from the time-varying content and single-view, occlusion-heavy observations further complicates the problem. As [1] pointed out, most methods struggle with realistic single-view videos. To disambiguate, some works [30–43] target specific scenes exploit domain knowledge like template models [44, 45]. A few recent works [46, 3, 47, 48] that tackle casual monocular videos of generic scenes propose to fuse information across frames, but only from a small temporal window, leading to unsatisfactory performance in challenging cases such as [1]. In [49] the scene is factorized into objects and relies on object-level tracking and appearance priors. Neural radiance fields [50–56] and 3D Gaussian Splatting [4, 57–59] are two promising approaches to novel view synthesis. The latter’s explicit point-based representation fits particularly well into the dynamic setting [14, 60, 26, 61, 27, 62–69]. We represent dynamic scenes with 3D Gaussians and use them for long-term, global aggregation.

Non-Rigid Structure-from-Motion. Geometric reconstruction of non-rigidly deforming scenes from a single RGB(D) camera has been a long-standing problem. [70–72, 44, 73, 74] focus on specific object categories or articulated shapes and register observations to template models [44]. Another group of methods [75–81] warp, align, and fuse scans of generic scenes. To model non-rigid deformations, state-of-the-art methods [77, 72, 78, 80] use Embedded Deformation Graphs [82], where dense transformations over the space are obtained from a sparse set of basis transformations. In our proposed *MoSca*, we draw inspiration from classic Embedded Graphs and extend them to effectively connect predictions from 2D foundation models to dynamic Gaussian splatting.

2D Vision Foundation Models. Recent years have witnessed great progress in developing large-scale pretrained vision foundation models [83–87] that serve as the basis for various downstream visual understanding tasks, ranging from image-level tasks such as visual question answering [88, 89, 87] to pixel-level tasks including segmentation [86], dense tracking [90], and monocular depth estimation [91, 92]. These models extract strong priors encoded in massive training data and demonstrate impressive generalization to in-the-wild test data. Such generic data priors are particularly useful in monocular video-based dynamic reconstruction, as they help disambiguate partial observations. Previous works [17, 20, 3, 48, 46, 49] have leveraged monocular depth [91, 92], optical flow [93], 2D-pixel tracks [94, 90], as well as object tracking [95] and image diffusion priors [96]. While most

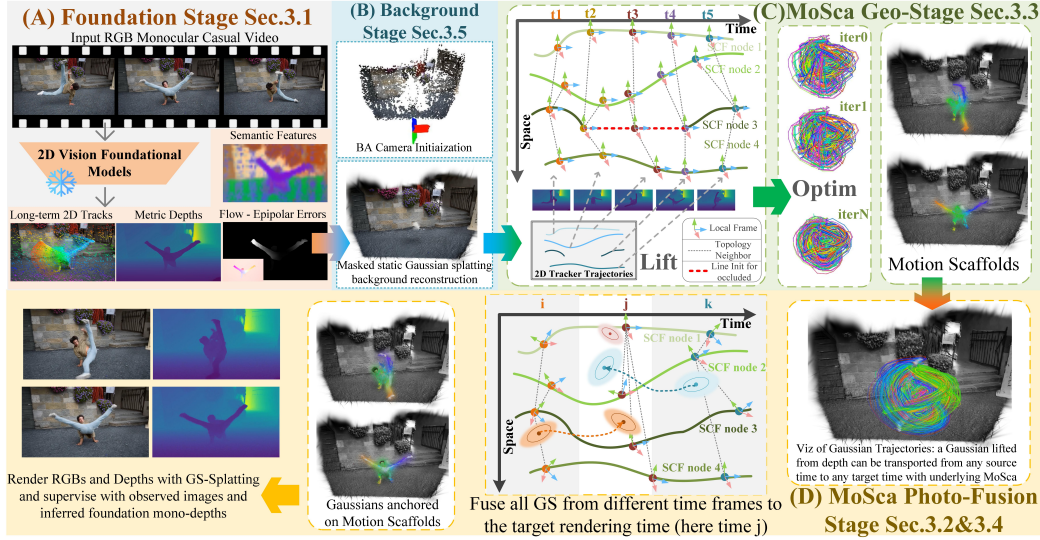


Figure 2: **Overview:** (A) Given a monocular casual video, we infer pre-trained 2D vision foundation models (Sec. 3.1). (B) The camera intrinsics and poses are solved using bundle adjustment, and the background is reconstructed via 3DGS [4] (Sec. 3.5). (C) Our proposed Motion Scaffold (*MoSca*) is lifted from 2D predictions and optimized with physics-inspired regularization and semantic cues (Sec. 3.3). (D) Gaussians are initialized from all timesteps, deformed with *MoSca* (Sec. 3.2), and fused globally to model the dynamic scene. The entire representation is rendered with Gaussian Splatting and optimized with photometric losses (Sec. 3.4).

existing methods directly use the 2D priors for regularization in image space, and often in isolation from each other, we propose to lift these 2D priors to 3D and fuse them synergetically.

3 Method

Given a casual monocular video of a dynamic scene with T frames $\mathcal{I} = [I_1, I_2, \dots, I_T]$, our goal is to reconstruct the geometry and appearance of the scene with a set of dynamic Gaussians, and to recover the focal length and poses of the camera if these quantities are unknown. Our key idea is to lift video input to a novel dynamic scene representation, which we name Motion Scaffolds (*MoSca*), where observations are fused **globally** and **geometrically** by leveraging powerful priors from pre-trained large vision foundation models and physics-inspired constraints.

MoSca (3.2) models the dynamics of the scene with a sparse graph of motion trajectories, which can be interpolated into a dense SE(3) deformation field. The appearance and geometry of the scene are represented by 3D Gaussians from all source timesteps, which can be transformed to and fused at any target timestep with the deformation field.

As shown in Fig. 2, we first acquire predictions from off-the-shelf 2D foundation models (3.1). To model the dynamic component, we initialize the motion graph by lifting these predictions to 4D and perform geometry optimization with physics-inspired objectives (3.3). We then spawn Gaussians at each frame and perform photometric optimization of the entire dynamic scene representation (3.4). A separate preprocessing stage solves camera poses, focal length, and static background (3.5).

3.1 Leveraging Priors from 2D Foundation Models

The partiality of the observation makes monocular dynamic reconstruction highly ill-posed. We propose to enhance the input with 2D foundation models, as they encode generic, highly generalizable priors of the visual world from massive amounts of training data. We propose to lift and fuse various 2D priors in a complementary manner in our *MoSca* framework. Specifically, we leverage 1) per-frame metric depth estimations [92] $\mathcal{D} = [D_1, D_2, \dots, D_T]$ that are relatively consistent across frames; 2) long-term 2D pixel trajectories [90] $\mathcal{T} = \{\tau^{(i)} = [(p_1^{(i)}, v_1^{(i)}), (p_2^{(i)}, v_2^{(i)}), \dots, (p_T^{(i)}, v_T^{(i)})]\}_i$, where $p_t^{(i)}, v_t^{(i)}$ represent the i -th trajectory’s 2D image coordinate and visibility at frame t , 3) per-frame epipolar error maps $\mathcal{M} = [E_1, E_2, \dots, E_T]$ [2] computed from RAFT [93] dense optical flow predictions, which indicate the likelihood of being in the dynamic foreground; and 4) DINO-v2 [85] semantic features maps $\mathcal{S} = [S_1, S_2, \dots, S_T]$ for additional cues on long-term correspondence.

3.2 Deformation Representation with *MoSca*

We first describe the modeling and reconstruction of the dynamic component, which we factorize into appearance plus geometry represented by 3D Gaussians, and their deformation across frames. We model the deformation of the scene with an explicit, compact, and structured representation, a graph, named 4D Motion Scaffold (*MoSca*) $(\mathcal{V}, \mathcal{E})$, inspired by classical Embedded Graph [82]

Motion Scaffold Graph Definition. Intuitively, the Motion Scaffold graph nodes $\mathcal{V} = \{\mathbf{v}^{(m)}\}_{m=1}^M$ are 6-DoF trajectories that describe the underlying low-rank, smooth motion of the scene, where the number of nodes M is much smaller ($100\times$, see Suppl. G) than the number of points required to represent the scene. Specifically, each node $\mathbf{v}^{(m)} \in \mathcal{V}$ consists of per-timestep rigid transformations $\mathbf{Q}_t^{(m)}$ and a global control radius $r^{(m)}$ that parameterizes a radial-basis-function (RBF) describing its influence on nearby points.

$$\mathbf{v}^{(m)} = ([\mathbf{Q}_1^{(m)}, \mathbf{Q}_2^{(m)}, \dots, \mathbf{Q}_T^{(m)}], r^{(m)}); \quad \mathbf{Q} = [\mathbf{R}, \mathbf{t}] \in SE(3), r \in \mathbb{R}^+, \quad (1)$$

Graph edges \mathcal{E} define the local neighborhood of trajectories and dictate how they influence other trajectories and 3D Gaussians. We first define the distance metric D_{curve} between nodes as their largest translation difference among all frames, then construct a k -nearest neighbor (KNN) graph based on it. Formally, we define the neighborhood of node $v^{(m)}$ as

$$\mathcal{E}(m) = \text{KNN}_{n \in \{1, \dots, M\}} [D_{\text{curve}}(m, n)], \quad D_{\text{curve}}(m, n) = \max_{t=1, 2, \dots, T} \|\mathbf{t}_t^{(m)} - \mathbf{t}_t^{(n)}\|, \quad (2)$$

where D_{curve} captures the global proximity between trajectories across all timesteps and considers the topology open and close situations.

SE(3) Deformation Field by Interpolating the Motion Scaffold Graph. Given *MoSca* $(\mathcal{V}, \mathcal{E})$, we can derive a dense deformation field by interpolating motions from nodes near the query point. Consider query position \mathbf{x} at time t_{src} , denote its nearest node at t_{src} as $\mathbf{v}^{(m^*)}$, we can efficiently compute its deformation to target time t_{dst} using nodes in the neighborhood of $v^{(m^*)}$. Formally,

$$\mathcal{W}(\mathbf{x}, \mathbf{w}; t_{\text{src}}, t_{\text{dst}}) = \text{DQB} \left(\{w_i, \mathbf{Q}_{t_{\text{dst}}}^{(i)} (\mathbf{Q}_{t_{\text{src}}}^{(i)})^{-1}\}_{i \in \mathcal{E}(m^*)} \right) \in SE(3), \quad m^* = \arg \min_m \|\mathbf{t}_{t_{\text{src}}}^{(m)} - \mathbf{x}\|, \quad (3)$$

where DQB [97–99] refers to Dual Quaternion Blending that smoothly interpolates elements in $SE(3)$ (See Supp. B), $\mathbf{w} = \{w_i\}$ are skinning weights computed from node RBFs parameterized by radius $r^{(i)}$. Formally,

$$w_i(\mathbf{x}, t_{\text{src}}) = \text{Normalize}_{i \in \mathcal{E}(m^*)} \left(\exp(-\|\mathbf{x} - \mathbf{t}_{t_{\text{src}}}^{(i)}\|_2^2 / 2r^{(i)}) \right) \in \mathbb{R}^+. \quad (4)$$

3.3 Initialization and Geometric Optimization of *MoSca*

One important contribution of this paper is to seamlessly connect *MoSca* with powerful 2D foundational models. The long-term 2D tracking \mathcal{T} together with the metric depth \mathcal{D} provide strong cues for \mathcal{V} . However, there is still a gap due to partial observations and unknown rotations \mathbf{R} , which we bridge by optimizing physics- and semantics-based objectives.

Initializing *MoSca* with Lifted 2D Priors. Given 2D tracks \mathcal{T} and epipolar error maps \mathcal{M} , we first identify foreground 2D tracks by thresholding their maximum epipolar error $e(\tau) = \max_{t=1 \dots T} E_t[p_t] \cdot v_t$ across visible timesteps. We then lift them to 3D using depth estimates \mathcal{D} at visible timesteps, and interpolate from nearby observations at occluded timesteps. Formally, we compute the 3D position \mathbf{p}_t at timestep t from 2D track $\tau = [(p_t, v_t)]_{t=1}^T$ as

$$\mathbf{p}_t = \begin{cases} \mathbf{W}_t \pi_{\mathbf{K}}^{-1}(p_t, D_t[p_t]), & \text{if } v_t = 1, \\ \text{LinearInterp}(\mathbf{p}_{\text{left}}, \mathbf{p}_{\text{right}}), & \text{if } v_t = 0, \end{cases} \quad (5)$$

where $\pi_{\mathbf{K}}^{-1}$ refers to back projection with camera intrinsic \mathbf{K} , \mathbf{W}_t refers to camera pose, $\mathbf{p}_{\text{left}}, \mathbf{p}_{\text{right}}$ refer to the lifted 3D positions from nearest visible timesteps before and after t . We initialize from each track a *MoSca* node $\mathbf{v}^{(i)}$ using lifted positions \mathbf{p}_t as the translation and identity as the rotation, i.e. $\mathbf{Q}_t^{(i)} = [\mathbf{I}, \mathbf{p}_t^{(i)}]$, as well as a pre-defined control radius r_{init} . In practice, we only keep a compact subset from the dense set of tracks by resampling nodes based on the curve distance (Eq. 2), please see Supp. C.1 for more details.

Geometry Optimization. Starting from the trivial initialization of rotations and invisible parts, we propose to propagate foundation priors from the observed portion of *MoSca* through the motion graph

topology. To this end, we optimize physics-inspired as-rigid-as-possible (ARAP) loss. Given two timesteps separated by interval Δ , we define ARAP loss $\mathcal{L}_{\text{arap}}$ as:

$$\mathcal{L}_{\text{arap}} = \sum_{t=1}^T \sum_{m=1}^M \sum_{n \in \hat{\mathcal{E}}(m)} \lambda_l \left| \|\mathbf{t}_t^{(m)} - \mathbf{t}_t^{(n)}\| - \|\mathbf{t}_{t+\Delta}^{(m)} - \mathbf{t}_{t+\Delta}^{(n)}\| \right| + \lambda_c \left\| \mathbf{Q}_t^{-1(n)} \mathbf{t}_t^{(m)} - \mathbf{Q}_{t+\Delta}^{-1(n)} \mathbf{t}_{t+\Delta}^{(m)} \right\|, \quad (6)$$

where $\hat{\mathcal{E}}$ refers to a multi-level hierarchical topology detailed in supp. C.2. The first term encourages the preservation of local metric lengths in the neighborhood and the second term preserves the local coordinate, involving the local frame \mathbf{Q} in the optimization. Please see supp. C.3 for more optimization details. We also enforce the temporal smoothness of the deformation by minimizing the velocity and acceleration:

$$\mathcal{L}_{\text{vel}} = \lambda_{\text{vel}} \sum_{t=1}^T \sum_{m=1}^M \|\mathbf{t}_t^{(m)} - \mathbf{t}_{t+1}^{(m)}\| + |\text{ang}(\mathbf{R}_t^{(m)} \mathbf{R}_{t+1}^{-1(m)})|, \quad (7)$$

$$\mathcal{L}_{\text{acc}} = \lambda_{\text{acc}} \sum_{t=1}^T \sum_{m=1}^M \|\mathbf{t}_t^{(m)} - 2\mathbf{t}_{t+1}^{(m)} + \mathbf{t}_{t+2}^{(m)}\| + |\text{ang}(\mathbf{R}_t^{(m)} \mathbf{R}_{t+1}^{-1(m)}) - \text{ang}(\mathbf{R}_{t+1}^{(m)} \mathbf{R}_{t+2}^{-1(m)})|, \quad (8)$$

where ang refers to the axes-angle of the rotation. We only optimize rotations and invisible 3D positions, leaving the visible 3D positions unchanged to prevent degeneration.

Exploiting Semantic Features. Pre-trained semantic features have shown promise in identifying long-term correspondence [100, 101]. We exploit DINOv2 [85] semantic features \mathcal{S} to counter prediction failures from long-term 2D trackers, as sometimes observed in challenging cases such as fast-moving parts. For each 2D trajectory τ , we compute the mean and variance of their semantic features $\{S_t[p_t]\}$. We filter out erroneous predictions by dropping trajectories with the top 10% highest feature variance. We also use semantic features to provide stronger signals for position optimization. One common tracker failure is to misclassify points as invisible, leading to coarsely initialized \mathbf{t}_t . Intuitively, we may find the point in the back-projected depth point cloud and use it to drag \mathbf{t}_t . Such points can be identified by matching pixel semantic features to the mean trajectory feature. Formally, we define a semantic loss:

$$\mathcal{L}_{\text{sem}} = \lambda_{\text{sem}} \sum_{t=1}^T \sum_{(i,m) \in \mathcal{R}_t} \|\mathbf{p}_t^{(i)} - \mathbf{t}_t^{(m)}\| \quad (9)$$

where \mathcal{R}_t refers to semantic matches between depth points and nodes, please see Supp. D for details. The final objective of geometric optimization is as follows:

$$\mathcal{L}_{\text{geo}} = \mathcal{L}_{\text{arap}} + \mathcal{L}_{\text{acc}} + \mathcal{L}_{\text{vel}} + \mathcal{L}_{\text{sem}}. \quad (10)$$

3.4 Dynamic Scene Representation and Photometric Optimization

Dynamic Scene Representation with Gaussians Deformed by *MoSca*. Geometric optimization of *MoSca* provides a reliable deformation field reconstruction of the scene, capable of transforming and fusing observations across timesteps. We complete the scene reconstruction with 3D Gaussians initialized from back-projected foreground depth points at all timesteps. Formally,

$$\mathcal{G} = \{(\mu_j, R_j, s_j, o_j, c_j; t_j^{\text{ref}}, \Delta \mathbf{w}_j)\}_{j=1}^N, \quad (11)$$

where the first five attributes are the center, rotation, non-isotropic scales, opacity, and spherical harmonics of 3DGS [4], and the latter two are tailored for *MoSca*. t_j^{ref} is the reference timestep, i.e. the timestep at which the Gaussian is initialized from the back-projected depth. $\Delta \mathbf{w}_j \in \mathbb{R}^K$ is the per Gaussian learnable skinning weight correction. To get the final complete geometry at a target timestep t , Gaussians from all timesteps will be deformed to timestep t and fused:

$$\mathcal{G}(t) = \{(\mathbf{T}_j(t)\mu_j, \mathbf{T}_j(t)R_j, s_j, o_j, c_j) \mid \mathbf{T}_j(t) = \mathcal{W}(\mu_j, \mathbf{w}(\mu_j, t_j^{\text{ref}}) + \Delta \mathbf{w}_j; t_j^{\text{ref}}, t)\}_{j=1}^N \quad (12)$$

where \mathcal{W} is the deformation field defined in Eq. 3, \mathbf{w} is the base skinning weight defined in Eq. 4.

Photometric Optimization and Scaffold Control. The above Gaussians can be rendered via any Gaussian Splatting-based differentiable renderer (including surface renderer [57]) and optimized with depth and RGB rendering losses together with the regularization losses from Sec. 3.3:

$$\mathcal{L} = \lambda_{\text{rgb}} \mathcal{L}_{\text{rgb}} + \lambda_{\text{dep}} \mathcal{L}_{\text{dep}} + \mathcal{L}_{\text{arap}} + \mathcal{L}_{\text{acc}} + \mathcal{L}_{\text{vel}}. \quad (13)$$

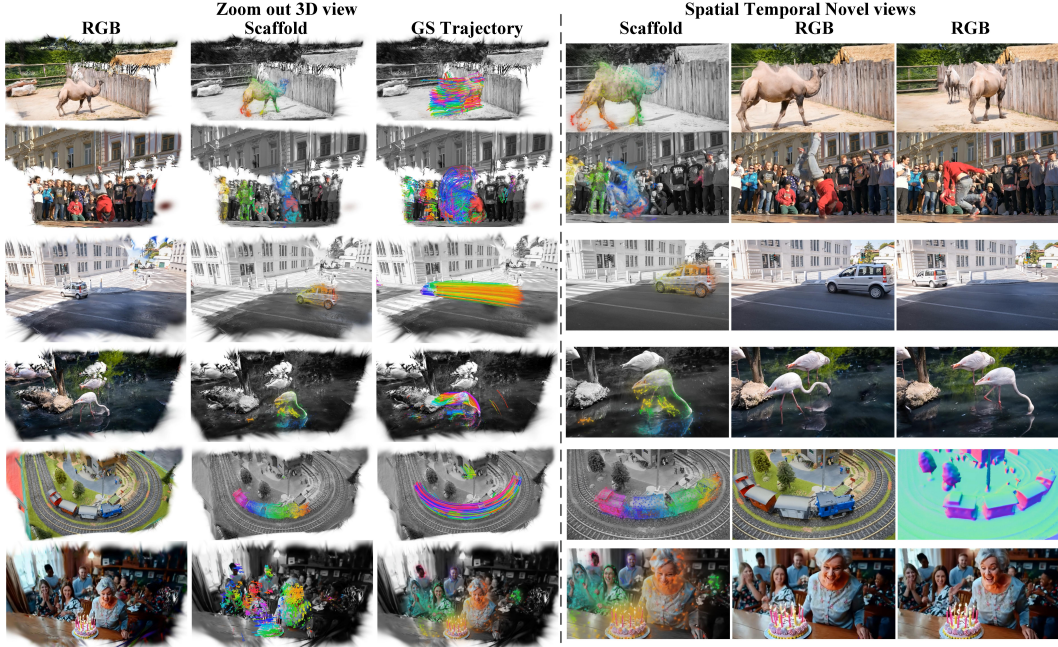


Figure 3: **In-the-wild Videos**: We show qualitative results on DAVIS [102] and the bottom row is an example from a SORA [103] generated video. The left is the zoomed-out 3D view of the reconstructed scene, the underlying *MoSca*, and the per-gaussian trajectories driven by *MoSca*. The right shows a closer viewpoint. Note *MoSca* also supports Gaussian Opacity Field [57] surface rendering as shown in the train normal map.

In addition to standard 3DGS Gaussian control techniques including gradient-based densification and reset-pruning simplification, we propose a novel control policy over the proposed *MoSca* nodes. Our policy is designed to address the under-representation of the scene, especially in regions with fine-grained, high-frequency motions, caused by a lack of scaffold nodes. To periodically density nodes, we select pixels from high-rendering loss regions, back-project them to 3D, subsample them, compute their initial node 6DoF trajectories using the current deformation field, and add them to the node set \mathcal{V} . Please see Supp. E for more details. We also prune nodes whose skinning weights towards all Gaussians fall under a threshold, indicating limited contribution to deformation modeling.

3.5 Solving Camera Parameters and Static Background

Finally, we describe the last component of the system that solves camera parameters and reconstructs the static background, followed by a recap of the complete pipeline.

Solving Camera Parameters/COLMAP-Free. By fully exploiting strong priors from 2D foundation models, our system can robustly solve camera parameters without off-the-shelf pose estimators such as COLMAP. Similar to the identification of dynamic 2D tracks, we identify the static background tracks from \mathcal{T} based on their epipolar errors. After initializing the FOV that best explains the tracking and depth with a smart parallel enumeration algorithm (detailed in Supp. F), we can optimize the camera poses and intrinsics jointly with re-projection errors on static tracks:

$$\mathcal{L}_{proj} = \lambda_{proj} \sum_{i \in |\mathcal{T}|} \sum_{a, b \in [1, T]} (v_a^{(i)} v_b^{(i)}) \cdot \left\| \pi_{\mathbf{K}} \left(\mathbf{W}_b^{-1} \mathbf{W}_a \pi_{\mathbf{K}}^{-1} (p_a^{(i)}, D_a[p_a^{(i)}]) \right) - p_b^{(i)} \right\|, \quad (14)$$

where $\pi_{\mathbf{K}}$ means projection with intrinsics \mathbf{K} involving the FOV, \mathbf{W}_t is the camera pose at time t . To account for errors in the depth estimation (in particular scale misalignment), we jointly optimize a correction to depth $D_a[p_a]$, consisting of per-frame global scaling factors and small per-pixel corrections, through a depth alignment loss:

$$\mathcal{L}_z = \lambda_z \sum_{i \in |\mathcal{T}|} \sum_{a, b \in [1, T]} (v_a^{(i)} v_b^{(i)}) D_{scale-inv} \left(\left[\mathbf{W}_b^{-1} \mathbf{W}_a \pi_{\mathbf{K}}^{-1} (p_a^{(i)}, D_a[p_a^{(i)}]) \right]_z, D_b[p_b^{(i)}] \right), \quad (15)$$

where $[\cdot]_z$ takes the z coordinate, $D_{scale-inv}(x, y) = |x/y - 1| + |y/x - 1|$. Our proposed simple yet efficient camera solver is critical for our system to work in the wild, where COLMAP may fail.

Table 1: Comparison on DyCheck [1], using metrics standard to the dataset.

	apple			block			paper-windmill			space-out		
	mPSNR	mSSIM	mLPIPS	mPSNR	mSSIM	mLPIPS	mPSNR	mSSIM	mLPIPS	mPSNR	mSSIM	mLPIPS
T-NeRF [1]	17.43	0.728	0.508	17.52	0.669	0.346	17.55	0.367	0.258	17.71	0.591	0.377
NSFF [17]	16.47	0.754	0.414	14.71	0.606	0.438	14.94	0.272	0.348	17.65	0.636	0.341
Nerfies [54]	17.54	0.750	0.478	16.61	0.639	0.389	17.34	0.378	0.211	17.79	0.622	0.303
HyperNeRF [55]	17.64	0.743	0.478	17.54	0.670	0.331	17.38	0.382	0.209	17.93	0.605	0.320
RoDynRF [2]	18.73	0.722	0.552	18.73	0.634	0.513	16.71	0.321	0.482	18.56	0.594	0.413
DynPoint [47]	17.78	0.743	-	17.67	0.667	-	17.32	0.366	-	17.78	0.603	-
PGDVS [48]	16.66	0.721	0.411	16.38	0.601	0.293	17.19	0.386	0.277	16.49	0.592	0.326
DyBluRF [28]	18.00	0.737	0.488	17.47	0.665	0.349	18.19	0.405	0.301	18.83	0.643	0.326
CTNeRF [29]	19.53	0.691	-	19.74	0.626	-	17.66	0.346	-	18.11	0.601	-
Ours	18.41	0.769	0.328	18.21	0.683	0.230	19.96	0.578	0.162	21.28	0.707	0.155
Ours GOF	18.29	0.765	0.322	18.40	0.687	0.246	19.70	0.565	0.156	21.17	0.704	0.152
Ours COLMAP-free	13.38	0.661	0.616	18.43	0.684	0.221	19.79	0.563	0.165	21.42	0.718	0.159
	spin			teddy			wheel			Mean across all scenes		
	mPSNR	mSSIM	mLPIPS	mPSNR	mSSIM	mLPIPS	mPSNR	mSSIM	mLPIPS	mPSNR	mSSIM	mLPIPS
T-NeRF [1]	19.16	0.567	0.443	13.71	0.570	0.429	15.65	0.548	0.292	16.96	0.577	0.379
NSFF [17]	17.26	0.540	0.371	12.59	0.537	0.527	14.59	0.511	0.331	15.46	0.551	0.396
Nerfies [54]	18.38	0.585	0.309	13.65	0.557	0.372	13.82	0.458	0.310	16.45	0.570	0.339
HyperNeRF [55]	19.20	0.561	0.325	13.97	0.568	0.350	13.99	0.455	0.310	16.81	0.569	0.332
RoDynRF [2]	17.41	0.484	0.570	14.33	0.536	0.613	15.20	0.449	0.478	17.10	0.534	0.517
DynPoint [47]	19.04	0.564	-	13.95	0.551	-	14.72	0.515	-	16.89	0.573	-
PGDVS [48]	18.49	0.590	0.247	13.29	0.516	0.399	12.68	0.429	0.429	15.88	0.548	0.340
DyBluRF [28]	18.20	0.541	0.400	14.61	0.572	0.425	16.26	0.575	0.325	17.37	0.591	0.373
CTNeRF [29]	19.79	0.516	-	14.51	0.509	-	14.48	0.430	-	17.69	0.531	-
Ours	20.46	0.692	0.193	15.62	0.612	0.286	15.12	0.493	0.238	18.44	0.648	0.227
Ours GOF	20.62	0.709	0.180	15.85	0.616	0.280	15.39	0.507	0.225	18.49	0.651	0.223
Ours COLMAP-free	20.20	0.650	0.188	14.40	0.573	0.314	13.04	0.399	0.314	17.24	0.607	0.283

Note that we will also optimize the camera poses \mathbf{W}_t throughout the rendering phases as well with photometric losses to further adjust the camera.

Reconstructing Static Background. We can compute foreground-background masks by thresholding the epipolar masks \mathcal{M} . We represent the static background with a standard 3DGS [4] $\mathcal{H} = \{(\mu_j, R_j, s_j, o_j, c_j)\}_{j=1}^H$, initialized by back-projecting background depth and optimized using standard rendering loss over masked background regions. The final renderable Gaussians are the union $\mathcal{G}(t) \cup \mathcal{H}$.

Full Pipeline. To summarize, our full pipeline consists of 4 steps: (A) Obtain predictions from off-the-shelf 2D vision foundational models (Sec. 3.1). Identify dynamic foreground and static background tracks and compute foreground masks. (B) Solve camera parameters and align the depth maps. Reconstruct the static background with Gaussians \mathcal{H} using standard 3DGS optimization. (Sec. 3.5) (C) Initialize *MoSca* with lifted dynamic 2D tracks and perform geometric optimization (Sec. 3.3) (D) Initialize the dynamic Gaussians \mathcal{G} and jointly optimize the complete representation including the static background Gaussians, dynamic foreground Gaussians, the deformation motion graph, and cameras (Sec. 3.4).

4 Results

Implementation Details. We use UniDepth [92] to compute metric depth estimation, use CoTracker-v2 [90] online mode to densely infer the long-term 2D-pixel tracks, use RAFT [93] to compute epipolar error maps and use DINO-v2 [85] to compute the semantic feature maps. Training camera poses are jointly optimized for both camera-unknown and camera-known cases. During inference, we follow the protocol in previous pose-free novel-view synthesis work [104] to obtain testing camera poses consistent with the trained renderable model, by first optimizing for testing poses that maximize PSNR on testing images. We use native 3DGS [4] as the default renderer and also report results from GOF [57] renderer.

Qualitative Results on in-the-wild Videos. We first verify the effectiveness of *MoSca* on in-the-wild videos in Fig. 3.

4.1 Comparison on Dycheck

The current most realistic and challenging monocular video novel view synthesis dataset is the iPhone Reality Check (DyCheck) [1] dataset, where generic, diverse dynamic scenes are captured with a hand-held iPhone with realistic camera motions for training, as well as two static cameras of large baseline for testing. For a fair comparison with previous methods that exploit noisy lidar depth from the dataset, we replace our estimated metric \mathcal{D} with lidar depth. The quantitative results are reported in Tab. 1 and the qualitative results are shown in Fig. 4. Due to the large deviation of testing views from the training camera trajectory, most per-frame depth warping methods directly fail, for example, Fig.9 of Casual-FVS [3]. Some recent Gaussian-based methods also fail since they depend on strong multi-view stereo cues (present in unnatural fast-moving camera motions) to reconstruct the scene. Fig.16 in 4DGaussian [60] illustrates such failures. As shown in Tab. 1, we outperform other SOTA methods, especially on LPIPS. We attribute such improvement to two factors: firstly, benefiting from

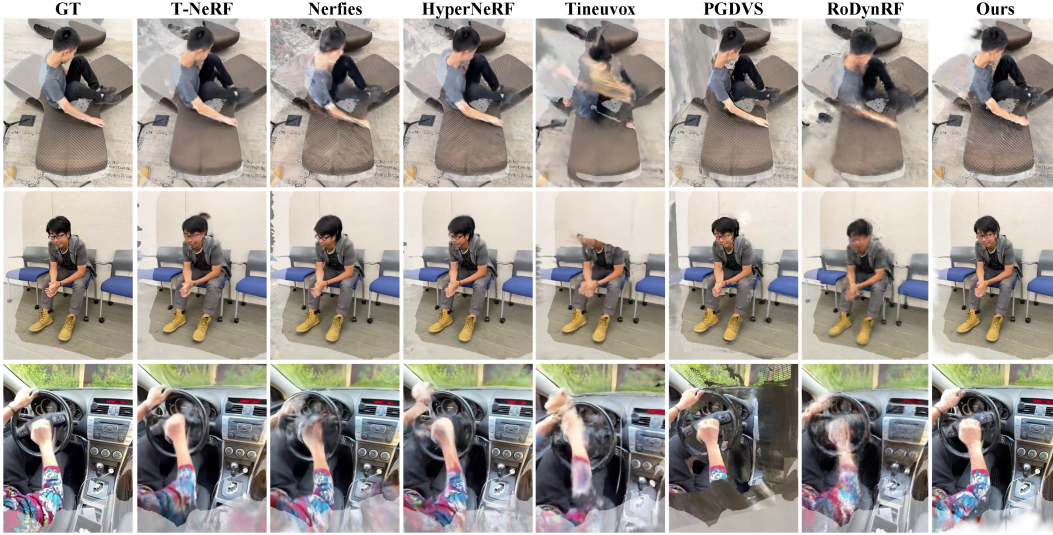


Figure 4: Visual comparison on DyCheck [1], the out-of co-visible mask area is masked with white color.

Table 2: Comparison on NVIDIA dataset with protocol from RoDynRF [2].

PSNR \setminus LPIPS	Jumping	Skating	Truck	Umbrella	Balloon1	Balloon2	Playground	Mean88								
D-NeRF [10]	22.36	0.193	22.48	0.323	24.10	0.145	21.47	0.264	19.06	0.259	20.76	0.277	20.18	0.164	21.49	0.232
NR-NeRF [21]	20.09	0.287	23.95	0.227	19.33	0.446	19.63	0.421	17.39	0.348	22.41	0.213	15.06	0.317	19.69	0.323
TiNeuVox [56]	20.81	0.247	23.32	0.152	23.86	0.173	20.00	0.355	17.30	0.353	19.06	0.279	13.84	0.437	19.74	0.285
HyperNeRF [55]	18.34	0.302	21.97	0.183	20.61	0.205	18.59	0.443	13.96	0.530	16.57	0.411	13.17	0.495	17.60	0.367
NSFF [17]	24.65	0.151	29.29	0.129	25.96	0.167	22.97	0.295	21.96	0.215	24.27	0.222	21.22	0.212	24.33	0.199
DynNeRF [20]	24.68	0.090	32.66	0.035	28.56	0.082	23.26	0.137	22.36	0.104	27.06	0.049	24.15	0.080	26.10	0.082
MonoNeRF [24]	24.26	0.091	32.06	0.044	27.56	0.115	23.62	0.180	21.89	0.129	27.36	0.052	22.61	0.130	25.62	0.106
4DGS [60]	21.93	0.269	24.84	0.174	23.02	0.175	21.83	0.213	21.32	0.185	18.81	0.178	18.40	0.196	21.45	0.199
Casual-FVS [3]	23.45	0.100	29.98	0.045	25.22	0.090	23.24	0.096	23.75	0.079	24.15	0.081	22.19	0.074	24.57	0.081
CTNeRF [29]	24.35	0.094	33.51	0.034	28.27	0.084	23.48	0.129	22.19	0.111	26.86	0.048	24.28	0.077	26.13	0.082
DynPoint [47]	24.69	0.097	31.34	0.045	29.30	0.061	24.59	0.086	22.77	0.099	27.63	0.049	25.37	0.039	26.53	0.068
RoDynRF [2]	25.66	0.071	28.68	0.040	29.13	0.063	24.26	0.089	22.37	0.103	26.19	0.054	24.96	0.048	25.89	0.067
RoDynRF [2] COLMAP-free	24.27	0.100	28.71	0.046	28.85	0.066	23.25	0.104	21.81	0.122	25.58	0.064	25.20	0.052	25.38	0.079
ours	25.21	0.083	32.77	0.033	28.22	0.090	24.41	0.092	23.26	0.092	28.90	0.042	23.05	0.060	26.55	0.070
Ours COLMAP-free	25.43	0.080	32.62	0.033	28.29	0.086	24.40	0.091	23.27	0.091	29.01	0.042	23.23	0.058	26.61	0.069

powerful pre-trained 2D long-term trackers, our *MoSca* representation models long-term motion trajectories, enabling the global aggregation of observations across all timesteps, which, in turn, leads to a more complete reconstruction; secondly, the sparse motion graph design of *MoSca* facilitates optimization. Compared to dense Gaussian geometries, its compact and smoothly interpolated motion nodes largely reduce the space of optimization. Its topology enables the effective propagation of information to unobserved regions through ARAP regularization.

4.2 Comparison on NVIDIA

We also evaluate on NVIDIA video dataset following the protocol in RoDynRF [2]. As reported in Tab. 2 and Fig. 5, we achieve high PSNR and very competitive LPIPS results. Our less significant improvement margin can be attributed to the relatively easier setting of RoDynRF [2] compared to DyCheck, where the smaller difference between testing and training views makes global fusion unnecessary and the forward-facing setup obviates the need for strong regularization on the occluded area. We would like to highlight the comparison with SOTA COLMAP-free dynamic rendering [2].

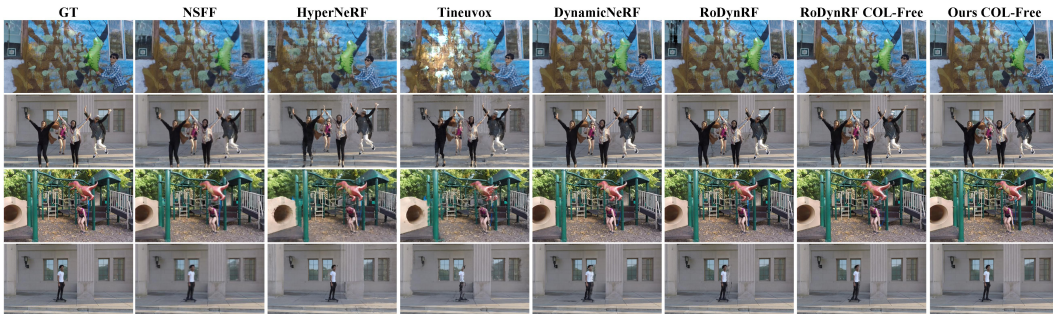


Figure 5: Visual comparison on NVIDIA dataset.

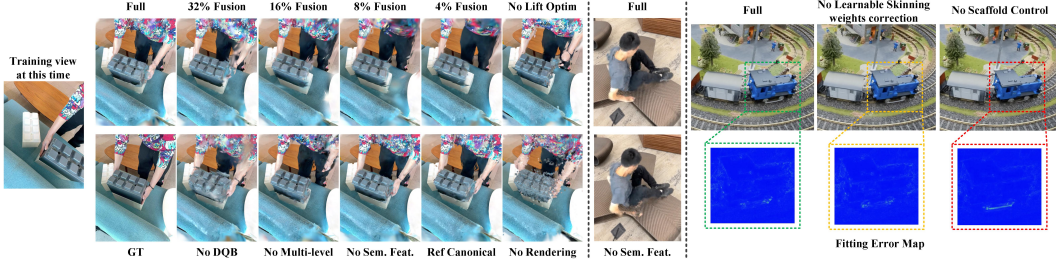


Figure 6: Ablation studies: A visual comparison of Tab. 3 is on the left; the middle column further showcases the semantic dragging can help on the arms where CoTracker [90] will fail. The right column shows the effect of skinning weight correction and scaffold node control.

Interestingly, our COLMAP-free version performs almost the same as initializing the pose from ground truth, whereas RoDynRF [2] has a performance drop.

4.3 Ablation Study

To verify the effectiveness of our design, we ablate our full framework and report the average performance on the DyCheck [1] dataset in Tab. 3. We verify the importance of fusing observations from many timesteps by filtering the Gaussians $\mathcal{G}(t)$ used for rendering with t^{ref} in Eq. 11 and Eq. 12. $N\%$ means only fusing observations from the neighboring $N\%$ timesteps. The performance drop with fewer timesteps being fused verifies our motivation to globally fuse information via *MoSca*. These ablations also demonstrate that *MoSca* is flexible and can be easily manipulated for varying the fusion temporal radius, which may be useful for extremely long videos. We also verify that purely initializing the Scaffold using Eq. 5 without geometric optimization (“No Lift Optim” in Tab. 3) is not enough. The photometric rendering stage is also necessary (shown as “No Rendering”). Other design details are also verified, including replacing DQB with Linear Blend Skinning (“No DQB”), not using multi-level ARAP topology $\hat{\mathcal{E}}$ in Eq. 6 (“No Multi-level”), and not using semantic drag as introduced at the end of Sec. 3.3 (“No Sem-Feat”).

We also verify the advantage of keeping the Gaussian μ, R at different time frames t^{ref} instead of first transporting them to a global canonical frame (“Ref in Canonical”) as suggested in Eq. 11,12. We observe a slight performance drop because the skinning weight in Eq. 4 is computed at the reference time t^{ref} , and saving the Gaussians at their born time as the reference would lead to more suitable skinning weights. Finally, we also justify the effectiveness of learnable skinning weights and scaffold node control on the right of Fig. 6, where small detailed deformation on the train can not be captured well without the node control.

Table 3: Ablation study on Dycheck

Ablation Methods	mPSNR	mSSIM	mLPIPS
full	18.44	0.648	0.227
Fusion 4%	18.15	0.640	0.248
Fusion 8%	18.29	0.646	0.240
Fusion 16%	18.38	0.648	0.233
Fusion 32%	18.34	0.644	0.231
No Lift Optim	18.05	0.640	0.240
No Rendering	17.00	0.597	0.334
No DQB	17.85	0.636	0.247
No Multi-level	18.30	0.642	0.232
No Sem-Feat.	18.40	0.647	0.227
Ref in Canonical	18.39	0.647	0.228

5 Limitations and Conclusion

Limitations. While *MoSca* achieves state-of-the-art performance on standard benchmarks and can work on some in-the-wild videos, several limitations remain: (1) Our method relies on good 2D long-term tracks and monocular metric depth estimation, indicating that the improvement of these 2D foundational models will benefit our performance. (2) Our current framework only deals with the reconstruction of areas that can be visible at some time frame. However, using large-scale 2D diffusion priors to hallucinate the area that is never visible is an important future direction of *MoSca*.

In summary, this paper attempts to make a tiny step towards reconstruction and rendering from monocular in-the-wild casual videos, which are widely available at an internet-level scale. We hope this small step may inspire future exploration toward understanding our dynamic physical world.

Broader Impact. This work may help artists and everyone to create spatial videos, making their memory more valuable. However, fake misleading videos and results can also be generated from the proposed method.

Acknowledgments and Disclosure of Funding

The authors appreciate the support of the gift from AWS AI to Penn Engineering’s ASSET Center for Trustworthy AI; and the support of the following grants: NSF IIS-RI 2212433, NSF FRR 2220868 awarded to UPenn, ARL grant W911NF-21-2-0104 and a Vannevar Bush Faculty Fellowship awarded to Stanford University.

The authors thank Minh-Quan Viet Bui and the authors of DyBluRF, Xiaoming Zhao and the authors of PGDVS for providing their per-scene evaluation metrics on DyCheck dataset.

References

- [1] Hang Gao, Ruilong Li, Shubham Tulsiani, Bryan Russell, and Angjoo Kanazawa. Monocular dynamic view synthesis: A reality check. *Advances in Neural Information Processing Systems*, 35:33768–33780, 2022.
- [2] Yu-Lun Liu, Chen Gao, Andreas Meuleman, Hung-Yu Tseng, Ayush Saraf, Changil Kim, Yung-Yu Chuang, Johannes Kopf, and Jia-Bin Huang. Robust dynamic radiance fields. In *Proceedings of the IEEE/CVF Conference on Computer Vision and Pattern Recognition*, pages 13–23, 2023.
- [3] Yao-Chih Lee, Zhoutong Zhang, Kevin Blackburn-Matzen, Simon Niklaus, Jianming Zhang, Jia-Bin Huang, and Feng Liu. Fast view synthesis of casual videos. *arXiv preprint arXiv:2312.02135*, 2023.
- [4] Bernhard Kerbl, Georgios Kopanas, Thomas Leimkühler, and George Drettakis. 3d gaussian splatting for real-time radiance field rendering. 2023.
- [5] C. Lawrence Zitnick, Sing Bing Kang, Matthew Uyttendaele, Simon Winder, and Richard Szeliski. High-quality video view interpolation using a layered representation. *ACM Transactions on Graphics (TOG)*, 2004.
- [6] Timo Stich, Christian Linz, Georgia Albuquerque, and Marcus Magnor. View and time interpolation in image space. *Computer Graphics Forum*, 2008.
- [7] Mojtaba Bermana, Karol Myszkowski, Hans-Peter Seidel, and Tobias Ritschel. X-fields: Implicit neural view-, light- and time-image interpolation. *SIGGRAPH Asia*, 2020.
- [8] Aayush Bansal, Minh Vo, Yaser Sheikh, Deva Ramanan, and Srinivasa Narasimhan. 4d visualization of dynamic events from unconstrained multi-view videos. In *Proceedings of the IEEE/CVF Conference on Computer Vision and Pattern Recognition (CVPR)*, 2020.
- [9] Tianye Li, Mira Slavcheva, Michael Zollhoefer, Simon Green, Christoph Lassner, Changil Kim, Tanner Schmidt, Steven Lovegrove, Michael Goesele, Richard Newcombe, et al. Neural 3d video synthesis from multi-view video. In *Proceedings of the IEEE/CVF Conference on Computer Vision and Pattern Recognition (CVPR)*, 2022.
- [10] Albert Pumarola, Enric Corona, Gerard Pons-Moll, and Francesc Moreno-Noguer. D-nerf: Neural radiance fields for dynamic scenes. In *Proceedings of the IEEE/CVF Conference on Computer Vision and Pattern Recognition*, pages 10318–10327, 2021.
- [11] Sara Fridovich-Keil, Giacomo Meanti, Frederik Warburg, Benjamin Recht, and Angjoo Kanazawa. K-planes: Explicit radiance fields in space, time, and appearance. *arXiv preprint arXiv:2301.10241*, 2023.
- [12] Ang Cao and Justin Johnson. Hexplane: A fast representation for dynamic scenes. *arXiv preprint arXiv:2301.09632*, 2023.
- [13] Benjamin Attal, Jia-Bin Huang, Christian Richardt, Michael Zollhoefer, Johannes Kopf, Matthew O’Toole, and Changil Kim. Hyperreel: High-fidelity 6-dof video with ray-conditioned sampling. In *Proceedings of the IEEE/CVF Conference on Computer Vision and Pattern Recognition (CVPR)*, 2023.
- [14] Jonathon Luiten, Georgios Kopanas, Bastian Leibe, and Deva Ramanan. Dynamic 3d gaussians: Tracking by persistent dynamic view synthesis. *arXiv preprint arXiv:2308.09713*, 2023.
- [15] Haotong Lin, Sida Peng, Zhen Xu, Tao Xie, Xingyi He, Hujun Bao, and Xiaowei Zhou. High-fidelity and real-time novel view synthesis for dynamic scenes. In *SIGGRAPH Asia Conference Proceedings*, 2023.
- [16] Jae Shin Yoon, Kihwan Kim, Orazio Gallo, Hyun Soo Park, and Jan Kautz. Novel view synthesis of dynamic scenes with globally coherent depths from a monocular camera. In *Proceedings of the IEEE/CVF Conference on Computer Vision and Pattern Recognition*, pages 5336–5345, 2020.

- [17] Zhengqi Li, Simon Niklaus, Noah Snively, and Oliver Wang. Neural scene flow fields for space-time view synthesis of dynamic scenes. In *Proceedings of the IEEE/CVF Conference on Computer Vision and Pattern Recognition*, pages 6498–6508, 2021.
- [18] Wenqi Xian, Jia-Bin Huang, Johannes Kopf, and Changil Kim. Space-time neural irradiance fields for free-viewpoint video. In *Proceedings of the IEEE/CVF Conference on Computer Vision and Pattern Recognition*, pages 9421–9431, 2021.
- [19] Chaoyang Wang, Ben Eckart, Simon Lucey, and Orazio Gallo. Neural trajectory fields for dynamic novel view synthesis. *arXiv preprint arXiv:2105.05994*, 2021.
- [20] Chen Gao, Ayush Saraf, Johannes Kopf, and Jia-Bin Huang. Dynamic view synthesis from dynamic monocular video. In *Proceedings of the IEEE/CVF International Conference on Computer Vision*, pages 5712–5721, 2021.
- [21] Edgar Treitschk, Ayush Tewari, Vladislav Golyanik, Michael Zollhöfer, Christoph Lassner, and Christian Theobalt. Non-rigid neural radiance fields: Reconstruction and novel view synthesis of a dynamic scene from monocular video. In *Proceedings of the IEEE/CVF International Conference on Computer Vision*, pages 12959–12970, 2021.
- [22] Tianhao Wu, Fangcheng Zhong, Andrea Tagliasacchi, Forrester Cole, and Cengiz Oztireli. D^2 nerf: Self-supervised decoupling of dynamic and static objects from a monocular video. *arXiv preprint arXiv:2205.15838*, 2022.
- [23] Liangchen Song, Anpei Chen, Zhong Li, Zhang Chen, Lele Chen, Junsong Yuan, Yi Xu, and Andreas Geiger. Nerfplayer: A streamable dynamic scene representation with decomposed neural radiance fields. *IEEE Transactions on Visualization and Computer Graphics*, 2023.
- [24] Fengrui Tian, Shaoyi Du, and Yueqi Duan. Mononerf: Learning a generalizable dynamic radiance field from monocular videos. In *Proceedings of the IEEE/CVF International Conference on Computer Vision*, pages 17903–17913, 2023.
- [25] Meng You and Junhui Hou. Decoupling dynamic monocular videos for dynamic view synthesis. *arXiv preprint arXiv:2304.01716*, 2023.
- [26] Ziyi Yang, Xinyu Gao, Wen Zhou, Shaohui Jiao, Yuqing Zhang, and Xiaogang Jin. Deformable 3d gaussians for high-fidelity monocular dynamic scene reconstruction. *arXiv preprint arXiv:2309.13101*, 2023.
- [27] Yiqing Liang, Numair Khan, Zhengqin Li, Thu Nguyen-Phuoc, Douglas Lanman, James Tompkin, and Lei Xiao. Gaufre: Gaussian deformation fields for real-time dynamic novel view synthesis. *arXiv preprint arXiv:2312.11458*, 2023.
- [28] Minh-Quan Viet Bui, Jongmin Park, Jihyong Oh, and Munchurl Kim. Dyblurf: Dynamic deblurring neural radiance fields for blurry monocular video. *arXiv preprint arXiv:2312.13528*, 2023.
- [29] Xingyu Miao, Yang Bai, Haoran Duan, Yawen Huang, Fan Wan, Yang Long, and Yefeng Zheng. Ctnerf: Cross-time transformer for dynamic neural radiance field from monocular video. *arXiv preprint arXiv:2401.04861*, 2024.
- [30] ShahRukh Athar, Zexiang Xu, Kalyan Sunkavalli, Eli Shechtman, and Zhixin Shu. Rignerf: Fully controllable neural 3d portraits. In *Proceedings of the IEEE/CVF Conference on Computer Vision and Pattern Recognition*, pages 20364–20373, 2022.
- [31] Chung-Yi Weng, Brian Curless, Pratul P Srinivasan, Jonathan T Barron, and Ira Kemelmacher-Shlizerman. Humannerf: Free-viewpoint rendering of moving people from monocular video. In *Proceedings of the IEEE/CVF Conference on Computer Vision and Pattern Recognition*, pages 16210–16220, 2022.
- [32] Alfredo Rivero, ShahRukh Athar, Zhixin Shu, and Dimitris Samaras. Rig3dgs: Creating controllable portraits from casual monocular videos. *arXiv preprint arXiv:2402.03723*, 2024.
- [33] Xinqi Liu, Chenming Wu, Jialun Liu, Xing Liu, Jinbo Wu, Chen Zhao, Haocheng Feng, Errui Ding, and Jingdong Wang. Gva: Reconstructing vivid 3d gaussian avatars from monocular videos, 2024.
- [34] Zhijing Shao, Zhaolong Wang, Zhuang Li, Duotun Wang, Xiangru Lin, Yu Zhang, Mingming Fan, and Zeyu Wang. Splattingavatar: Realistic real-time human avatars with mesh-embedded gaussian splatting. *arXiv preprint arXiv:2403.05087*, 2024.

- [35] David Svitov, Pietro Morerio, Lourdes Agapito, and Alessio Del Bue. Haha: Highly articulated gaussian human avatars with textured mesh prior. *arXiv preprint arXiv:2404.01053*, 2024.
- [36] Jing Wen, Xiaoming Zhao, Zhongzheng Ren, Alexander G Schwing, and Shenlong Wang. Gomavatar: Efficient animatable human modeling from monocular video using gaussians-on-mesh. *arXiv preprint arXiv:2404.07991*, 2024.
- [37] Jiahui Lei, Yufu Wang, Georgios Pavlakos, Lingjie Liu, and Kostas Daniilidis. Gart: Gaussian articulated template models. *arXiv preprint arXiv:2311.16099*, 2023.
- [38] Muhammed Kocabas, Jen-Hao Rick Chang, James Gabriel, Oncel Tuzel, and Anurag Ranjan. Hugs: Human gaussian splats. *arXiv preprint arXiv:2311.17910*, 2023.
- [39] Shoukang Hu and Ziwei Liu. Gauhuman: Articulated gaussian splatting from monocular human videos. *arXiv preprint arXiv:2312.02973*, 2023.
- [40] Liangxiao Hu, Hongwen Zhang, Yuxiang Zhang, Boyao Zhou, Boning Liu, Shengping Zhang, and Liqiang Nie. Gaussianavatar: Towards realistic human avatar modeling from a single video via animatable 3d gaussians. *arXiv preprint arXiv:2312.02134*, 2023.
- [41] Yufan Chen, Lizhen Wang, Qijing Li, Hongjiang Xiao, Shengping Zhang, Hongxun Yao, and Yebin Liu. Monogaussianavatar: Monocular gaussian point-based head avatar. *arXiv preprint arXiv:2312.04558*, 2023.
- [42] Zhiyin Qian, Shaofei Wang, Marko Mihajlovic, Andreas Geiger, and Siyu Tang. 3dgs-avatar: Animatable avatars via deformable 3d gaussian splatting. *arXiv preprint arXiv:2312.09228*, 2023.
- [43] Mingwei Li, Jiachen Tao, Zongxin Yang, and Yi Yang. Human101: Training 100+ fps human gaussians in 100s from 1 view. *arXiv preprint arXiv:2312.15258*, 2023.
- [44] Federica Bogo, Angjoo Kanazawa, Christoph Lassner, Peter Gehler, Javier Romero, and Michael J Black. Keep it smpl: Automatic estimation of 3d human pose and shape from a single image. In *European Conference on Computer Vision*, pages 561–578. Springer, 2016.
- [45] Luan Tran and Xiaoming Liu. Nonlinear 3d face morphable model. In *Proceedings of the IEEE conference on computer vision and pattern recognition*, pages 7346–7355, 2018.
- [46] Zhengqi Li, Qianqian Wang, Forrester Cole, Richard Tucker, and Noah Snavely. Dynibar: Neural dynamic image-based rendering, 2023.
- [47] Kaichen Zhou, Jia-Xing Zhong, Sangyun Shin, Kai Lu, Yiyuan Yang, Andrew Markham, and Niki Trigoni. Dynpoint: Dynamic neural point for view synthesis. *Advances in Neural Information Processing Systems*, 36, 2024.
- [48] Xiaoming Zhao, Alex Colburn, Fangchang Ma, Miguel Angel Bautista, Joshua M. Susskind, and Alexander G. Schwing. Pseudo-generalized dynamic view synthesis from a video, 2024.
- [49] Wen-Hsuan Chu, Lei Ke, and Katerina Fragkiadaki. Dreamscene4d: Dynamic multi-object scene generation from monocular videos. *arXiv preprint arXiv:2405.02280*, 2024.
- [50] Ben Mildenhall, Pratul P Srinivasan, Matthew Tancik, Jonathan T Barron, Ravi Ramamoorthi, and Ren Ng. Nerf: Representing scenes as neural radiance fields for view synthesis. *Communications of the ACM*, 65(1):99–106, 2021.
- [51] Jonathan T Barron, Ben Mildenhall, Matthew Tancik, Peter Hedman, Ricardo Martin-Brualla, and Pratul P Srinivasan. Mip-nerf: A multiscale representation for anti-aliasing neural radiance fields. In *Proceedings of the IEEE/CVF International Conference on Computer Vision*, pages 5855–5864, 2021.
- [52] Anpei Chen, Zexiang Xu, Andreas Geiger, Jingyi Yu, and Hao Su. Tensorf: Tensorial radiance fields. In *Computer Vision—ECCV 2022: 17th European Conference, Tel Aviv, Israel, October 23–27, 2022, Proceedings, Part XXXII*, pages 333–350. Springer, 2022.
- [53] Thomas Müller, Alex Evans, Christoph Schied, and Alexander Keller. Instant neural graphics primitives with a multiresolution hash encoding. *arXiv preprint arXiv:2201.05989*, 2022.
- [54] Keunhong Park, Utkarsh Sinha, Jonathan T Barron, Sofien Bouaziz, Dan B Goldman, Steven M Seitz, and Ricardo Martin-Brualla. Nerfies: Deformable neural radiance fields. In *Proceedings of the IEEE/CVF International Conference on Computer Vision*, pages 5865–5874, 2021.

- [55] Keunhong Park, Utkarsh Sinha, Peter Hedman, Jonathan T Barron, Sofien Bouaziz, Dan B Goldman, Ricardo Martin-Brualla, and Steven M Seitz. Hypernerf: A higher-dimensional representation for topologically varying neural radiance fields. *arXiv preprint arXiv:2106.13228*, 2021.
- [56] Jiemin Fang, Taoran Yi, Xinggang Wang, Lingxi Xie, Xiaopeng Zhang, Wenyu Liu, Matthias Nießner, and Qi Tian. Fast dynamic radiance fields with time-aware neural voxels. In *SIGGRAPH Asia 2022 Conference Papers*, pages 1–9, 2022.
- [57] Zehao Yu, Torsten Sattler, and Andreas Geiger. Gaussian opacity fields: Efficient and compact surface reconstruction in unbounded scenes. *arXiv preprint arXiv:2404.10772*, 2024.
- [58] Leonid Keselman and Martial Hebert. Approximate differentiable rendering with algebraic surfaces. In *European Conference on Computer Vision*, pages 596–614. Springer, 2022.
- [59] Leonid Keselman and Martial Hebert. Flexible techniques for differentiable rendering with 3d gaussians. *arXiv preprint arXiv:2308.14737*, 2023.
- [60] Guanjun Wu, Taoran Yi, Jiemin Fang, Lingxi Xie, Xiaopeng Zhang, Wei Wei, Wenyu Liu, Qi Tian, and Xinggang Wang. 4d gaussian splatting for real-time dynamic scene rendering. *arXiv preprint arXiv:2310.08528*, 2023.
- [61] Bardienus P Duisterhof, Zhao Mandi, Yunchao Yao, Jia-Wei Liu, Mike Zheng Shou, Shuran Song, and Jeffrey Ichnowski. Md-splatting: Learning metric deformation from 4d gaussians in highly deformable scenes. *arXiv preprint arXiv:2312.00583*, 2023.
- [62] Zeyu Yang, Hongye Yang, Zijie Pan, Xiatian Zhu, and Li Zhang. Real-time photorealistic dynamic scene representation and rendering with 4d gaussian splatting. *arXiv preprint arXiv:2310.10642*, 2023.
- [63] Kai Katsumata, Duc Minh Vo, and Hideki Nakayama. An efficient 3d gaussian representation for monocular/multi-view dynamic scenes. *arXiv preprint arXiv:2311.12897*, 2023.
- [64] Youtian Lin, Zuozhuo Dai, Siyu Zhu, and Yao Yao. Gaussian-flow: 4d reconstruction with dynamic 3d gaussian particle. *arXiv preprint arXiv:2312.03431*, 2023.
- [65] Zhan Li, Zhang Chen, Zhong Li, and Yi Xu. Spacetime gaussian feature splatting for real-time dynamic view synthesis. *arXiv preprint arXiv:2312.16812*, 2023.
- [66] Agelos Kratimenos, Jiahui Lei, and Kostas Daniilidis. Dynmf: Neural motion factorization for real-time dynamic view synthesis with 3d gaussian splatting. *arXiv preprint arXiv:2312.00112*, 2023.
- [67] Yi-Hua Huang, Yang-Tian Sun, Ziyi Yang, Xiaoyang Lyu, Yan-Pei Cao, and Xiaojuan Qi. Sc-gs: Sparse-controlled gaussian splatting for editable dynamic scenes. *arXiv preprint arXiv:2312.14937*, 2023.
- [68] Devikalyan Das, Christopher Wewer, Raza Yunus, Eddy Ilg, and Jan Eric Lenssen. Neural parametric gaussians for monocular non-rigid object reconstruction. *arXiv preprint arXiv:2312.01196*, 2023.
- [69] Yuanxing Duan, Fangyin Wei, Qiyu Dai, Yuhang He, Wenzheng Chen, and Baoquan Chen. 4d gaussian splatting: Towards efficient novel view synthesis for dynamic scenes. *arXiv preprint arXiv:2402.03307*, 2024.
- [70] Volker Blanz and Thomas Vetter. A morphable model for the synthesis of 3d faces. In *Proceedings of the 26th Annual Conference on Computer Graphics and Interactive Techniques*, pages 187–194, 1999.
- [71] Varun Ramakrishna, Takeo Kanade, and Yaser Sheikh. Reconstructing 3d human pose from 2d image landmarks. In *European Conference on Computer Vision*, pages 573–586. Springer, 2012.
- [72] Michael Zollhöfer, Matthias Nießner, Shahram Izadi, Christoph Rehmann, Christopher Zach, Matthew Fisher, Chenglei Wu, Andrew Fitzgibbon, Charles Loop, Christian Theobalt, et al. Real-time non-rigid reconstruction using an rgb-d camera. *ACM Transactions on Graphics (ToG)*, 33(4):1–12, 2014.
- [73] Gengshan Yang, Deqing Sun, Varun Jampani, Daniel Vlasic, Forrester Cole, Huiwen Chang, Deva Ramanan, William T Freeman, and Ce Liu. Lasr: Learning articulated shape reconstruction from a monocular video. In *Proceedings of the IEEE/CVF Conference on Computer Vision and Pattern Recognition*, pages 4925–4935, 2021.
- [74] Gengshan Yang, Minh Vo, Natalia Neverova, Deva Ramanan, Andrea Vedaldi, and Hanbyul Joo. Banmo: Building animatable 3d neural models from many casual videos. In *Proceedings of the IEEE/CVF Conference on Computer Vision and Pattern Recognition*, pages 22247–22257, 2022.

- [75] Brian Curless and Marc Levoy. A volumetric method for building complex models from range images. In *Proceedings of the 23rd annual conference on Computer graphics and interactive techniques*, pages 303–312, 1996.
- [76] Hao Li, Robert W Sumner, and Mark Pauly. Global correspondence optimization for non-rigid registration of depth scans. *Computer Graphics Forum*, 27(5):1421–1430, 2008.
- [77] Mingsong Dou, Jonathan Taylor, Henry Fuchs, Andrew Fitzgibbon, and Shahram Izadi. 3d scanning deformable objects with a single rgbd sensor. In *Proceedings of the IEEE Conference on Computer Vision and Pattern Recognition*, pages 493–501, 2015.
- [78] Richard A Newcombe, Dieter Fox, and Steven M Seitz. Dynamicfusion: Reconstruction and tracking of non-rigid scenes in real-time. In *Proceedings of the IEEE conference on computer vision and pattern recognition*, pages 343–352, 2015.
- [79] Wei Gao and Russ Tedrake. Surfelwarp: Efficient non-volumetric single view dynamic reconstruction. In *Robotics: Science and Systems (RSS)*, 2018.
- [80] Aljaz Bozic, Pablo Palafox, Michael Zollöfer, Angela Dai, Justus Thies, and Matthias Nießner. Neural non-rigid tracking. In *Advances in Neural Information Processing Systems*, volume 33, pages 18765–18775, 2020.
- [81] Yilun Du, Yanan Zhang, Hong-Xing Yu, Joshua B Tenenbaum, and Jiajun Wu. Neural radiance flow for 4d view synthesis and video processing. In *2021 IEEE/CVF International Conference on Computer Vision (ICCV)*, pages 14304–14314. IEEE Computer Society, 2021.
- [82] Robert W Sumner, Johannes Schmid, and Mark Pauly. Embedded deformation for shape manipulation. In *ACM siggraph 2007 papers*, pages 80–es. 2007.
- [83] Rishi Bommasani, Drew A Hudson, Ehsan Adeli, Russ Altman, Simran Arora, Sydney von Arx, Michael S Bernstein, Jeannette Bohg, Antoine Bosselut, Emma Brunskill, et al. On the opportunities and risks of foundation models. *arXiv preprint arXiv:2108.07258*, 2021.
- [84] Alec Radford, Jong Wook Kim, Chris Hallacy, Aditya Ramesh, Gabriel Goh, Sandhini Agarwal, Girish Sastry, Amanda Askell, Pamela Mishkin, Jack Clark, et al. Learning transferable visual models from natural language supervision. In *International conference on machine learning*, pages 8748–8763. PMLR, 2021.
- [85] Maxime Oquab, Timothée Darcet, Théo Moutakanni, Huy Vo, Marc Szafraniec, Vasil Khalidov, Pierre Fernandez, Daniel Haziza, Francisco Massa, Alaaeldin El-Nouby, et al. Dinov2: Learning robust visual features without supervision. *arXiv preprint arXiv:2304.07193*, 2023.
- [86] Alexander Kirillov, Eric Mintun, Nikhila Ravi, Hanzi Mao, Chloe Rolland, Laura Gustafson, Tete Xiao, Spencer Whitehead, Alexander C Berg, Wan-Yen Lo, et al. Segment anything. In *Proceedings of the IEEE/CVF International Conference on Computer Vision*, pages 4015–4026, 2023.
- [87] OpenAI. Gpt-4 technical report, 2023. <https://openai.com/research/gpt-4>.
- [88] Haotian Liu, Chunyuan Li, Yuheng Li, and Yong Jae Lee. Improved baselines with visual instruction tuning. *arXiv preprint arXiv:2310.03744*, 2023.
- [89] Haotian Liu, Chunyuan Li, Qingyang Wu, and Yong Jae Lee. Visual instruction tuning. *Advances in neural information processing systems*, 36, 2024.
- [90] Nikita Karaev, Ignacio Rocco, Benjamin Graham, Natalia Neverova, Andrea Vedaldi, and Christian Rupprecht. Cotracker: It is better to track together. *arXiv preprint arXiv:2307.07635*, 2023.
- [91] Shariq Farooq Bhat, Reiner Birkel, Diana Wofk, Peter Wonka, and Matthias Müller. Zoedepth: Zero-shot transfer by combining relative and metric depth. *arXiv preprint arXiv:2302.12288*, 2023.
- [92] Luigi Piccinelli, Yung-Hsu Yang, Christos Sakaridis, Mattia Segu, Siyuan Li, Luc Van Gool, and Fisher Yu. Unidepth: Universal monocular metric depth estimation. *arXiv preprint arXiv:2403.18913*, 2024.
- [93] Zachary Teed and Jia Deng. Raft: Recurrent all-pairs field transforms for optical flow. In *Computer Vision—ECCV 2020: 16th European Conference, Glasgow, UK, August 23–28, 2020, Proceedings, Part II 16*, pages 402–419. Springer, 2020.
- [94] Adam W. Harley, Zhaoyuan Fang, and Katerina Fragkiadaki. Particle video revisited: Tracking through occlusions using point trajectories. 2022.

- [95] Ho Kei Cheng and Alexander G Schwing. Xmem: Long-term video object segmentation with an atkinson-shiffrin memory model. In *European Conference on Computer Vision*, pages 640–658. Springer, 2022.
- [96] Robin Rombach, Andreas Blattmann, Dominik Lorenz, Patrick Esser, and Björn Ommer. High-resolution image synthesis with latent diffusion models. In *Proceedings of the IEEE/CVF conference on computer vision and pattern recognition*, pages 10684–10695, 2022.
- [97] Yan-Bin Jia. Dual quaternions.
- [98] Ladislav Kavan, Steven Collins, Jiří Žára, and Carol O’Sullivan. Skinning with dual quaternions. In *Proceedings of the 2007 symposium on Interactive 3D graphics and games*, pages 39–46, 2007.
- [99] Konstantinos Daniilidis. Hand-eye calibration using dual quaternions. *The International Journal of Robotics Research*, 18(3):286–298, 1999.
- [100] Yunzhou Song, Jiahui Lei, Ziyun Wang, Lingjie Liu, and Kostas Daniilidis. Track everything everywhere fast and robustly, 2024.
- [101] Narek Tumanyan, Assaf Singer, Shai Bagon, and Tali Dekel. Dino-tracker: Taming dino for self-supervised point tracking in a single video, 2024.
- [102] Jordi Pont-Tuset, Federico Perazzi, Sergi Caelles, Pablo Arbeláez, Alex Sorkine-Hornung, and Luc Van Gool. The 2017 davis challenge on video object segmentation. *arXiv preprint arXiv:1704.00675*, 2017.
- [103] Tim Brooks, Bill Peebles, Connor Holmes, Will DePue, Yufei Guo, Li Jing, David Schnurr, Joe Taylor, Troy Luhman, Eric Luhman, Clarence Ng, Ricky Wang, and Aditya Ramesh. Video generation models as world simulators. 2024.
- [104] Yang Fu, Sifei Liu, Amey Kulkarni, Jan Kautz, Alexei A. Efros, and Xiaolong Wang. Colmap-free 3d gaussian splatting. 2023.

A More Visual Results in Supplemental Video

We encourage the readers to watch our supplemental video for more visual results.

B Dual Quaternion Blending

Since the motion is discretely approximated by sparse nodes in *MoSca*, it’s important to define good interpolation both spatially and temporally. To this end, we use Dual Quaternion Blending (DQB) [98] to mix two or more $SE(3)$ elements on the $SE(3)$ manifold. Similar to the unit quaternion representation of $SO(3)$, the unit dual quaternion is a representation of $SE(3)$ using 8 numbers by adding a dual part. Please see [97–99] for details. Given L rigid transformations and corresponding blending weights, the interpolated motion is:

$$\text{DQB}(\{(w_1, \mathbf{Q}_1), \dots, (w_L, \mathbf{Q}_L)\}) = \frac{w_1 \hat{\mathbf{q}}_1 + \dots + w_L \hat{\mathbf{q}}_L}{\|w_1 \hat{\mathbf{q}}_1 + \dots + w_L \hat{\mathbf{q}}_L\|_{DQ}}, \quad (16)$$

where $\hat{\mathbf{q}}$ is the dual quaternion representation of \mathbf{Q} and $\|\cdot\|_{DQ}$ is the dual norm [98]. Different from linear blend skinning, DQB is a manifold interpolation that always produces an element in $SE(3)$.

C Details of *MoSca* Lifting

C.1 Resample of Nodes

In Sec. 3.1 when inferring the foundational 2D long-term tracker, we will sample around $20k$ queries across random frames from the video. One reason for sampling so many queries is the Co-Tracker [90] performance depends on the sampling, we have to sample enough to maintain the high accuracy of Co-Tracker. However, the number of our *MoSca* nodes is usually far less than $20k$, so we have to resample nodes from these $20k$ raw co-tracker queried trajectories. Given many lifted 3D curves, we use the curve distance in Eq. 2 to compute a dense distance matrix. We sort all these curves by how many time steps it has been visible. Using such order we can iterate over all curves and include the curve to the sub-sampled set if it is far away from any included curves with a threshold unit. This spatial unit controls the overall density of the nodes and is empirically set to a predefined fixed value. Depending on the scene, usually, the number of subsampled nodes is around 100 – 4000 vs the raw $20k$ Co-Tracker output.

C.2 Multi-Level Topology

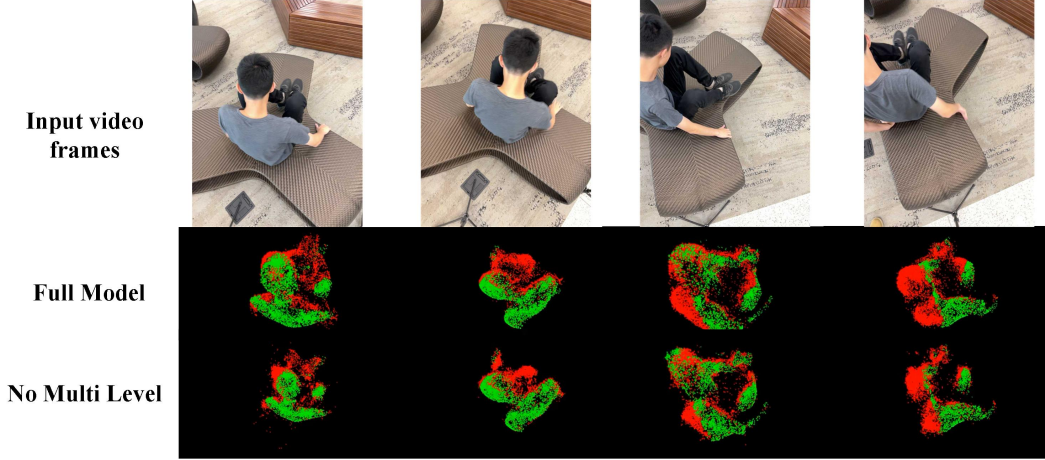


Figure 7: In the first row we show the input views that have challenging truncation and occlusion, for where we can not trivially back-project the 2D tracker. These challenging areas also justify the necessity of the geometry optimization stage in Sec. 3.3. The second and third row is the visualization of the scaffold nodes after geometric optimization with ARAP loss, where the green nodes are visible from the input view and red nodes are invisible and solved by the optimization.

As shown in our ablation study in Sec. 4.3, the multi-level topology is critical when using ARAP regularization, especially when the object is largely truncated and occluded. Fig. 7 gives more examples of it. Note that without regularizing on multi-level topology, the invisible occluded nodes will not be optimized to reasonable configurations. To augment the topology \mathcal{E} defined in Eq. 2, we simply sub-sample the nodes with the different spatial units used in the re-sample algorithm introduced above in Supp. C.1. All level neighboring pairs jointly union together and form the augmented multi-level topology $\hat{\mathcal{E}}$ for computing ARAP losses in Eq. 6.

C.3 Multi-Stage ARAP optimization

As shown in Fig. 7, there may be largely occluded areas where we don't know the monocular depth so we can't lift them into 3D. As in Eq. 5, these points are initialized using line segments. The geometric optimization proposed in Sec. 3.3 aims to solve the location of these nodes as well as the unknown local frames which the 2D tracker can not provide. However, we observe that directly optimizing these two together may not be the most efficient way. Recall Eq. 6:

$$\mathcal{L}_{\text{arap}} = \sum_{t=1}^T \sum_{m=1}^M \sum_{n \in \hat{\mathcal{E}}(m)} \lambda_l \left(\|\mathbf{t}_t^{(m)} - \mathbf{t}_t^{(n)}\| - \|\mathbf{t}_{t+\Delta}^{(m)} - \mathbf{t}_{t+\Delta}^{(n)}\| \right) + \lambda_c \left\| \mathbf{Q}_t^{-1(n)} \mathbf{t}_t^{(m)} - \mathbf{Q}_{t+\Delta}^{-1(n)} \mathbf{t}_{t+\Delta}^{(m)} \right\|, \quad (17)$$

where the first term does not depend on the local coordinates. We observe that only optimizing the left term can quickly converge to reasonable locations of occluded nodes. With this optimized location, we can analytically solve a simple Procrustes problem to find the analytical optimal rotation change of the local frame with respect to the finest level topology. These local frames are then used as initialization of local frames \mathbf{R} and finally all physical deformation losses are optimized together.

D Details of Leveraging Semantic Features

We observe that even the most advanced 2D trackers may fail on some fast-moving parts such as the human arms in Fig. 6-middle and Fig. 7. The failure usually behaves as (1) lost track once the arm has disappeared, or (2) confusion between similar colored areas such as the boy’s hair and the legs. This motivates us to exploit foundational semantic features to rescue such failures as proposed in Sec. 3.3. Given per-frame DINO-v2 [85], we first do a global PCA across all time frames and get 64 dim semantic features. For every 2D track trajectory, we collect the mean and variance of the semantic features across all the time when it’s visible. The high semantic variance is likely indicating a foreground-background failure case (2) of the tracker that maps points from one semantic part to another, as in Sec. 3.3, we filter out these 2D tracklets.

We also rescue case (1) by dragging the *MoSca* during the geometric optimization. In some tracker failure cases, the 2D tracker can track when one part is visible but loses track after it’s occluded, which means in the scaffold node, this part already corresponds to some existing node, but due to the 2D tracker lost track, it may not be at the correct location once the part re-appear. Such observation motivates us to “reuse” the nodes as much as possible. At each time frame, we back-project all the foreground pixels into 3D, compute their distance to the nearest scaffold nodes at this time frame, and mark depth points as uncovered via thresholding these distances. We can do similar thresholding to the nodes to mark unused nodes. We then find the K-nearest unused nodes of every uncovered depth point in the feature space and check whether their semantic feature distance is within 3 times the node feature STD. These K-nearest semantic pairs form \mathcal{R}_t at time t in Eq. 9 and we compute these semantic pair sets for each time frame to apply semantic drag regularization, whose effect is shown in Fig. 6-middle.

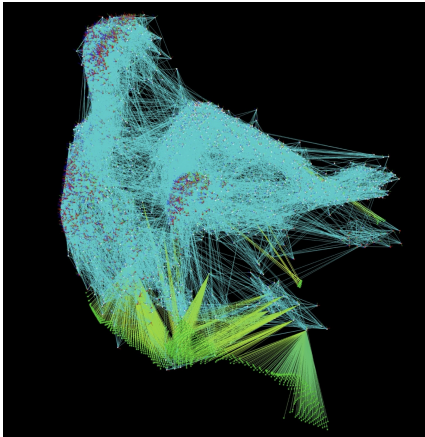


Figure 8: Visualization of the semantic dragging pairs on the boy-spinning example (Fig. 7). The green points are the uncovered arm depth points where CoTracker [90] may fail. The green edges indicate which unused node these depth points are semantically matched to. The blue edges are the visualization of current *MoSca* that is being optimized.

E Details of Node Densification in Photometric Optimization

Similar to the densification and pruning in standard 3DGS [4], we also design a complexity control of *MoSca*. While one may guess since all the Gaussians are anchored on *MoSca* and the nodes can simply collect the per Gaussian gradient norm via the skinning topology, it turns out that the gradient of Gaussian sometimes aligns with the geometry, especially on the boundary of the object as shown in Fig. 9. This Gaussian gradient does not well indicate the under-representation of deformation. Another choice may be to record the gradient norm of each node itself. However, the gradient of the scaffold nodes is not simply decided by photometric rendering error. The ARAP loss and regularization also determine the node gradient, leaving it unpractical.

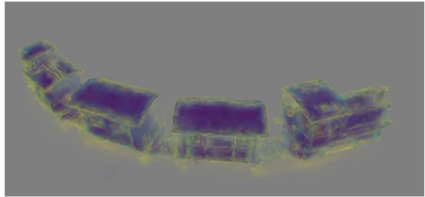


Figure 9: Gradient norm of Gaussians (yellow is large and purple is low)

So we design the simple policy as introduced in Sec. 3.4 to increase the scaffold complexity. In later iterations of the photometric optimization when the standard 3DGS control has been extensively applied, we periodically compute the rendering error map for all the frames in the input video. Then we threshold the errors and identify the error masks. We select the time frame with the largest error and back-project all the pixels within the error mask to 3D. These back-projected points are sub-sampled and are initialized with an identical local frame at the current time. Then these subsampled points along with the local frame can be deformed by the current *MoSca* with Eq. 3 and we append them as new nodes to *MoSca*.

F Details of FOV initialization

We simplify the camera projection model to contain only one degree of freedom, the Field of View (one shared focal length). Since there is only one degree of freedom, we can linearly search to enumerate the best initial FOV guess that best explains the estimated tracking and depth. Given an FOV and any two-time frames, we can

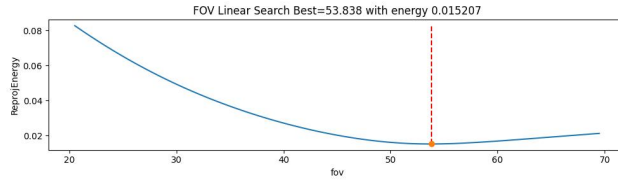


Figure 10: FOV initialization enumeration energy

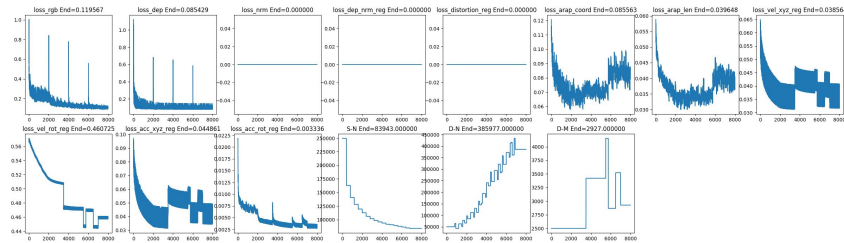


Figure 11: An example of the joint fine-tuning stage loss curves. The three empty curves are placeholders for GOF [57] surface regularization which is not used in this example. **Note that the last three sub-plots correspond to the number of Gaussians in the static background, the number of Gaussians in the dynamic foreground, and finally the number of *MoSca* nodes.** The curves of the deformation regularizations have sharp changes due to the proposed scaffold node control policy modifying the topology.

use the depth to un-project the co-visible pixels on the static 2D trajectories between these two frames and solve analytically a $SIM(3)$ Procrustes problem to find the best relative pose of the two cameras and then use this pose to compute the re-projection error between the depth. After computing all possible time pairs given a fixed FOV, we can build and reproject energy for it. So we can enumerate all possible FOVs by linear search and find the optimal FOV with the minimum energy. Note all the above operations can be efficiently computed in parallel and the overall enumeration can be done within seconds. Fig. 10 shows an example of such enumeration on one DyCheck [1] iPhone sequence. Note that the above algorithm only provides an initial FOV guess, which will be further optimized in the global BA as introduced in Sec. 3.5.

G Other Details

We also show an example of the optimization loss curves and the number of Gaussians and scaffold nodes in Fig. 11 of the Dragon scene shown in the teaser Fig. 1, illustrating the compactness of *MoSca* with only around $3K$ nodes vs around $400K$ Gaussians for the dynamic component.

All the experiments and qualitative results reported in the paper and video can be achieved on one Nvidia GPU with only 16GB VRAM. Depending on the scene size and rendering backend (GOF [57] may be slower when scaled up), most fitting can be done in around 0.5-2 hours.